A NAPE–LRRK2 metabolic axis controls lysosomal homeostasis in Parkinson's disease

Francesca Palese[1,2*], Carmela Giachino[3], Sylvie Syan[1], Giuliana Ottonello[2], Giulia Sciandrone[4], Carolina Filipponi[4], Michele Lai[4], Andrea Armirotti[2], Michela Deleidi[3], Chiara Zurzolo[1,5*]

[1] Institut Pasteur, Université Paris Cité, CNRS UMR 3691, Membrane Traffic and Pathogenesis, F-75015 Paris, France

[2] Analytical Chemistry Facility, Istituto Italiano di Tecnologia, Via Morego 30, 16163 Genova, Italy.

[3] Institut Imagine, INSERM UMR1163 Paris Cite' University, 24 boulevard du Montparnasse, 75015, Paris, France

[4] Retrovirus Center, Department of Translational Research and New Technologies in Medicine and Surgery, University of Pisa, Pisa, Italy

[5] Department of Molecular Medicine and Medical Biotechnology, University of Naples Federico II, Naples, Italy

Email: Francesca.palese@pasteur.fr

Chiara.zurzolo@pasteur.fr

Author Contributions: Conceptualization: FP; Methodology: FP, CG, SS, GO, GS; Investigation: FP; Visualization: FP; Supervision: FP, ML, MD, AA; Funding acquisition: FP, CZ; Writing – original draft: FP; Writing – review & editing: FP, MD, CZ.

Competing Interest Statement: No competing interests.

Keywords: N-acylphosphatidylethanolamines (NAPE), LRRK2, Lysosomes, Lipid signaling, Parkinson's disease

Abstract

N-acylphosphatidylethanolamines (NAPEs) are atypical glycerophospholipids that accumulate in response to cellular stress, yet their roles beyond serving as precursors of fatty-acid ethanolamines (FAEs) remain largely unexplored. Here, we identify NAPEs as endogenous regulators of leucine-rich repeat kinase 2 (LRRK2), a master controller of lysosomal homeostasis and a genetic driver of Parkinson's disease. We show that increasing NAPE synthesis or blocking their hydrolysis inhibits LRRK2 kinase activity, enhances lysosomal function, and promotes the clearance of α-synuclein aggregates. Conversely, cells in which NAPE hydrolysis is enhanced display increased LRRK2 activation and lysosomal dysfunction. Importantly, in induced pluripotent stem cell–derived dopaminergic neurons carrying the LRRK2-G2019S variant, pharmacological inhibition of NAPE-PLD – the enzyme that degrades NAPEs – restores lysosomal activity and favors the clearance of preformed α-synuclein fibrils. Together, our findings identify NAPEs as previously unrecognized lipid regulators of LRRK2 signaling and lysosomal function, revealing a metabolic axis with therapeutic potential in Parkinson's disease.

Main Text

Introduction

N-acylphopshpatidylethanolamines (NAPEs) are low-abundance glycerophospholipids present in the membranes of all eukaryotic cells (1). They are synthesized through the transfer of an acyl group from phosphatidylcholine (PC) to phosphatidylethanolamine (PE) by calcium-independent phospholipase A and acyltransferases (PLAATs), which maintain basal NAPE levels (2), or by the calcium-dependent phospholipase PLA2G4E, which is activated in a stimulus-dependent manner to markedly increase NAPE production under pathological conditions (3, 4). NAPEs are hydrolyzed by the NAPE-specific phospholipase D (NAPE-PLD) (5, 6), generating fatty-acid ethanolamines (FAEs) and phosphatidic acid (PA).

FAEs mediate diverse physiological and pathological processes, including neurotransmission (7, 8), pain (9), energy homeostasis (10, 11) and inflammation (12, 13), through receptors such as cannabinoid receptors, TRPV1, GPR119 and PPAR-α. Consequently, NAPEs have traditionally been viewed mainly as precursors of FAEs rather than molecules with intrinsic biological activity. However, NAPE production is dynamically regulated by physiological (7, 14) and pathological stimuli (15–17) including ischemia (18), excitotoxicity (19) and neurotoxic insults (20–22). Under pathological conditions, NAPE levels often exceed those of FAEs, suggesting functions independent of downstream FAE signaling. Consistent with this idea, NAPEs have been shown to stabilize cellular membranes (23, 24), regulate membrane fusion (25) and lipid raft organization (26), thereby influencing protein association at the membranes (27, 28). Notably, NAPEs accumulate in the brains of mouse models of Parkinson's disease (PD) (21, 29), where they exert neuroprotective effects against 6-OHDA-induced toxicity (29). In contrast, circulating NAPE levels are decreased in the plasma of female PD patients (30).

These observations suggest that NAPEs may participate in adaptive lipid response to neuronal stress in PD. However, the molecular mechanisms through which NAPEs influence neuronal survival and disease-relevant pathways remain largely unknown.

One potential link between NAPE signaling and PD pathogenesis is the regulation of membrane-associated signaling proteins that control endolysosomal trafficking. Among there, leucine-rich

repeat kinase 2 (LRRK2) has emerged as a central regulator of endolysosomal dynamics and lysosomal function whose dysregulation is strongly linked to PD (31). Mutations in the *LRRK2* gene represent one of the most common genetic causes of PD, accounting for ~1-2% of all cases worldwide but reaching up to 30-40% of cases in certain founder populations (32). Previous work recruitment (28). Here, we investigate the molecular mechanism underlying NAPE-mediated neuroprotection, focusing on LRRK2 regulation. We find that NAPE accumulation — either through enhanced synthesis or inhibition of their hydrolysis — reduces LRRK2 kinase activity and improves lysosomal function, thereby promoting the clearance of α-synuclein pre-formed fibrils (PFFs). Conversely, overexpression of the hydrolyzing enzyme NAPE-PLD increases LRRK2 protein abundance and kinase activity, impairs lysosomal function, and decreases α-synuclein PFF clearance.

Importantly, in induced pluripotent stem cell-derived dopaminergic neurons carrying the hyperactivating LRRK2-G2019S variant, pharmacological inhibition of NAPE-PLD restores lysosomal activity and enhances α-synuclein PFF clearance. Together, these findings identify NAPEs as previously unrecognized regulators of LRRK2 activity and lysosomal function, with direct implications for PD pathogenesis, and highlight NAPE-PLD inhibitors as promising therapeutic candidates.

Results

NAPEs accumulation potentiates lysosomal activity via LRRK2 inhibition

To investigate the effects of NAPE accumulation in a neuronal context, we genetically modulated NAPE metabolism in catecholaminergic SH-SY5Y cells using two approaches: (i) overexpression of the synthesizing enzyme PLA2G4E and (ii) knockdown of the hydrolyzing enzyme NAPE-PLD (**Fig. 1A**). Using a CRISPR-Cas9 strategy we obtained a partial knockdown (KD), resulting in an approximatively 30% reduction in *NAPE-PLD* mRNA (**Fig. 1B**), and a 30-50% decrease in protein levels (depending on the technique used for the measurement, **Fig. 1C, D**). This led to a 30% increase in total NAPE levels (**Fig. 1E**). Consistent with a hypomorphic condition, no significant compensatory changes were observed in *PLA2G4E* mRNA or protein (**Fig. S1 A-C**).

In parallel, SH-SY5Y cells overexpressing (OE) the synthesizing enzyme PLA2G4E (33) displayed a massive upregulation of both mRNA (~$3x10^4$-fold) and protein (~30-fold) levels **(Fig 1F-H**). In line with a strong potentiation of the synthetic pathway, these cells exhibited a 70-fold increase in total NAPE content (**Fig. 1 I**). Notably, NAPE-PLD protein levels were downregulated in these conditions (**Fig. S1 E, F**), likely reflecting an adaptive response aimed at limiting excessive FAE production.

Previous studies in NAPE-PLD knockout mouse brains and in NAPE-PLD silenced neuronal cells showed a reduced LRRK2 fraction associated with membranes (28); however, the underlying mechanisms and functional consequences of this observation were not investigated. Here, we show that both NAPE-PLD KD and PLA2G4E OE reduce LRRK2 abundance in neuronal cells (**Fig. 2 A**). Moreover, the LRRK2 kinase activity measured by western blot using phosphorylation of Rab8a at T72 — a LRRK2-specific phosphorylation site — was lowered in both NAPE-PLD KD and PLA2G4E OE cells compared with WT SH-SY5Y cells (**Fig. 2 C**). Furthermore, we observed diminished LRRK2 localization at lysosomes (**Fig. 2B, D**) in both NAPE-PLD KD and PLA2G4E OE cells relative to WT cells. Given that LRRK2 can be recruited to lysosomes in response to lysosomal stress or damage (34, 35) this is consistent with improved lysosomal health under conditions of NAPE accumulation.

LRRK2 is an established regulator of lysosomal degradative activity. LRRK2 knockout or kinase inhibition has been shown to increase lysosomal proteolytic activity, whereas pathogenic, hyperactive LRRK2 mutations associated with PD impair lysosomal degradative activity (36–38). In accordance with an inhibitory function of LRRK2 on lysosomal activity, we observed increased lysosomal cathepsin B activity in cells where NAPEs accumulate and LRRK2 is decreased in a NAPE-dose-dependent manner (+20% in NAPE-PLD KD cells and + 31% in PLA2G4E OE cells; **Fig. 2E**). Interestingly, treatment with the calcium ionophore ionomycin - which is reported to stimulate the production of NAPEs (39)(**Fig. S2A**)- further improved lysosomal activity in both NAPE-enriched cell lines (**Fig. S2B**).

Since increased lysosomal enzyme activity can also occur as a compensatory response to impaired autophagosome-lysosome fusion, we assessed autophagic flux to avoid misinterpretation. Cells were treated with the autophagosome-lysosome fusion inhibitor Bafilomycin A1, and p62-Lamp1 colocalization was measured. Under baseline conditions we did not observe any significant difference among cell lines (**Fig. S3A**). As expected for autophagic flux, Bafilomycin A1 treatment resulted in increased accumulation of p62-Lamp1-positive structures in all conditions (**Fig. S3A**), indicating that autophagosome-lysosome fusion is functional in our cell models. These results support the conclusion that NAPE accumulation enhances lysosomal activity rather than reflecting impaired autophagic flux.

Furthermore, no differences were observed in TFEB nuclear localization or total levels across cell lines (**Fig. S3B, C**), indicating that NAPE-mediated lysosomal protection operates independently of TFEB activation, the master transcriptional regulator of lysosomal biogenesis (40).

NAPEs-enriched cells clear exogenous pre-formed α-synuclein fibrils more efficiently

We next investigated the effect of NAPE accumulation under pathological conditions, specifically following exposure to exogenous pre-formed α-synuclein (α-syn) fibrils (PFFs). α-Syn PFFs are well known to induce lysosomal stress and activate LRRK2 kinase activity in neurons (41, 42), thereby establishing a negative feedback loop on lysosomal activity. Interestingly, following overnight exposure of WT, NAPE-PLD KD and PLA2G4E OE cells to α-syn PFFs we detected a ~2-fold increase in LRRK2 protein levels in WT cells, whereas the increase was very modest in NAPE-enriched cells (+4% and +34% in NAPE-PLD KD and PLA2G4E OE cells, respectively; **Fig. 3 A**). These data support NAPE-mediated negative regulation of LRRK2 protein levels, in addition to reduced LRRK2 recruitment to lysosomes (**Fig. 3 B**). Furthermore, consistent with their enhanced lysosomal activity, both NAPE-PLD KD and PLA2G4E OE cells showed fewer α-syn aggregates after overnight PFF treatment, followed by a 6-h washout period, compared with WT SH-SY5Y cells (**Fig. 3 C**).

Lysosomal activity and α-synuclein fibrils clearance are impaired in NAPE-PLD-overexpressing cells

To strengthen these findings, we next generated SH-SY5Y cells overexpressing NAPE-PLD. In these cells, *NAPE-PLD* mRNA and protein levels increased by approximately 10^3-fold and 5-fold respectively (**Fig. 4 A-D**), a condition expected to markedly enhance NAPE hydrolysis at cellular membranes under basal condition (43)(**Fig. 4 A**). In line with the non-rate limiting role of NAPE-PLD in FAE biosynthesis (44), no major compensatory effects were detected in PLA2G4E expression levels (**Fig. S4 A-C**).

157 In contrast to NAPE-enriched cells, NAPE-PLD OE cells exhibited elevated LRRK2 protein levels
158 and kinase activity (**Fig. 4 E, F**). These cells displayed markedly reduced cathepsin B activity
159 relative to WT (77% of WT levels; **Fig. 4H**), consistent with LRRK2's known suppression of
160 lysosomal hydrolases. Notably, ionomycin treatment -which boosts NAPE production and, in
161 NAPE-PLD-overexpressing cells, is expected to promote robust FAEs generation- failed to rescue
162 cathepsin B activity (**Fig. 4H**). This suggests that lysosomal impairment is driven by altered NAPE
163 levels rather than by FAE or phosphatidic acid byproducts. Importantly, the lysosomal impairment
164 observed in NAPE-PLD OE cells was reversed by treatment with LEI-401 (a NAPE-PLD inhibitor)
165 (**Fig. S5 A**). Furthermore, when LEI-401 and ionomycin treatments were combined, lysosomal
166 activity reached 136% of WT levels, consistent with maximal NAPE accumulation (**Fig. 4H**). In line
167 with our observation of elevated LRRK2 activity in NAPE-PLD OE cells, overnight treatment with
168 the LRRK2 pharmacological inhibitor MLi-2, not only improved lysosomal activity in WT cells, but it
169 also rescued the lysosomal impairment detected in NAPE-PLD OE cells (**Fig. S6**), supporting the
170 conclusion that NAPE levels regulate lysosomal activity through modulation of LRRK2 abundance
171 and kinase activity.

172 Following Bafilomycin A1 treatment, NAPE-PLD OE cells showed reduced p62-Lamp1
173 colocalization compared to WT cells (**Fig. S7A**), indicating impaired autophagosome-lysosome
174 fusion consistent LRRK2 overexpression (45). Moreover, these cells exhibited elevated TFEB
175 levels in both cytosolic and nuclear compartments (**Fig. S7B-E**), suggesting a compensatory
176 response attempting restore lysosomal homeostasis.

177 Finally, following overnight treatment with α-syn PFFs, LRRK2 protein levels increased further in
178 NAPE-PLD OE cells (~3-fold relative to untreated WT cells and ~1.5-fold relative to WT cells treated
179 with α-syn; **Fig. 5A**), in contrast to NAPE-enriched cells, where the α-syn-induced increase in
180 LRRK2 levels was contained. Consistent with reduced lysosomal degradative capacity, the number
181 of α -syn aggregates after a 6-hour washout period were higher in NAPE-PLD OE SH-SY5Y cells
182 than in WT cells (**Fig. 5 B**). Together, these results identify a previously unrecognized role for
183 NAPEs in regulating lysosomal activity and the handling of protein aggregates in neurons through
184 modulation of LRRK2 activity.

185 ***NAPE-PLD inhibition restores lysosomal activity and α-synuclein fibril clearance in G2019S-***
186 ***LRRK2 dopaminergic neurons***

187 We next tested the therapeutic potential of NAPE-PLD inhibition in human iPSC-derived
188 dopaminergic neurons (hDANs) carrying the PD-linked LRRK2-G2019S mutation and their isogenic
189 control line. This mutation is a gain-of-function variant that increases LRRK2 kinase activity (46),
190 resulting in impaired lysosomal function (47). Between differentiation day 21-24, when hDANs
191 express neuronal markers (TUJ1 and MAP2) and the dopaminergic marker tyrosine hydroxylase
192 (TH; **Fig. S8 A, B**), cells were treated overnight with the NAPE-PLD inhibitor LEI-401 prior to
193 measuring lysosomal activity using the Magic Red Cathepsin B assay. Consistent with LRRK2-
194 mediated lysosomal impairment, G2019S-LRRK2 neurons displayed fewer active lysosomes than
195 isogenic controls, an effect rescued by LEI-401 treatment (**Fig. 6 A, B**). These findings indicate that
196 increasing NAPE levels through NAPE-PLD inhibition counteracts LRRK2 hyperactivation and
197 restore lysosomal function.

198 We next assessed whether this rescue translated into improved handling of pathological α-syn.
199 hDANs were treated with α-syn PFFs in the presence or absence of LEI-401. Both G2019S-LRRK2
200 neurons and isogenic controls efficiently internalized PFFs after 48 h incubation (**Fig. 6 C**), with

comparable baseline uptake between genotypes. Strikingly, LEI-401 treatment significantly reduced the number of intracellular α-syn aggregates per cell in both mutant and control neurons compared to untreated conditions, demonstrating enhanced aggregate clearance. Together, these results establish NAPE-PLD inhibition as a mechanism to restore lysosomal function and promote pathological protein clearance in human dopaminergic neurons. These findings identify NAPEs as upstream modulators of LRRK2-dependent lysosomal dysfunction and highlight NAPE-PLD as a promising therapeutic target for Parkinson's disease and related neurodegenerative disorders characterized by impaired lysosomal proteostasis.

Discussion

In the present study, we identify NAPEs as previously unrecognized lipid regulators of LRRK2 signaling and lysosomal function in neuronal cells and human dopaminergic neurons. By genetically and pharmacologically manipulating NAPE synthesis and hydrolysis, we define a lipid-kinase axis in which NAPE accumulation (i) restrains LRRK2 kinase activity, (ii) preserves lysosomal degradative capacity, and (iii) promotes α-synuclein aggregate clearance, whereas NAPE depletion has the opposite effect. These findings provide a mechanistic framework linking stress-induced NAPE production to endolysosomal homeostasis and suggest that NAPE-PLD is a viable target to counteract LRRK2 hyperactivation in PD.

LRRK2 is increasingly recognized as a stress-responsive regulator of lysosomes, recruited to enlarged or damaged lysosomes where it phosphorylates Rab GTPases and constrains lysosomal degradative activity (36, 48–50). Our data place NAPEs upstream of this pathway: elevating NAPEs by PLA2G4E overexpression or NAPE-PLD knockdown reduces LRRK2 abundance and Rab8a T72 phosphorylation and enhances lysosomal cathepsin B activity, whereas NAPE-PLD overexpression increases LRRK2 protein and kinase output and impairs lysosomal function. These manipulations support a model in which NAPE levels set a "lipid tone" that tunes LRRK2 activation and, consequently, lysosomal capacity (35, 36, 38). Mechanistically, this aligns with prior observations that NAPE accumulation reduces LRRK2 partitioning to membrane fractions, whereas enhanced NAPE hydrolysis promotes membrane association (28). NAPEs stabilize and remodel membranes (23, 24), regulate fusion (25), and alter lipid raft organization (26), so changes in local NAPE content could influence LRRK2 recruitment to membrane microdomains supporting its activation. Unaltered TFEB responses in NAPE-enriched models suggest direct membrane effects, stabilizing fusion curvature or disrupting LRRK2-Rab raft recruitment. Our data indeed do not yet discriminate whether NAPEs act directly on LRRK2 and its scaffolds or indirectly through altered Rab or organelle organization, but the tight correlation between NAPE levels, LRRK2 activity, and lysosomal performance supports a functionally integrated module.

NAPE-PLD hydrolyzes NAPEs into bioactive FAEs such as OEA and PEA, as well as phosphatidic acid (PA), both of which can influence lysosomal function (51, 52). FAEs can promote lysosomal biogenesis via PPAR-α–TFEB signaling (53, 54),while PA modulates membrane properties in a concentration-dependent manner (55). However, our data argue that NAPEs themselves are the primary drivers of the observed effects. In NAPE-PLD-overexpressing cells, ionomycin-induced NAPE synthesis, which increases FAEs and PA, fails to restore lysosomal activity, whereas pharmacological NAPE accumulation via LEI-401 robustly enhances it. Although LRRK2 inhibition (MLi-2) partially rescues lysosomal defects, maximal restoration requires combined NAPE elevation, indicating both LRRK2-dependent and -independent contributions. Together, these findings support a model in which NAPEs act as stress-inducible membrane lipids with autonomous

247 regulatory functions, effectively constraining LRRK2 activity and tuning lysosomal competence
248 under proteotoxic conditions.

249 Pathogenic LRRK2 mutations, particularly G2019S, enhance kinase activity and drive lysosomal
250 dysfunction, impaired autophagy, and α-synuclein accumulation (38, 47). While LRRK2 kinase
251 inhibitors can partially restore lysosomal function and reduce α-synuclein burden (56), our results
252 extend this paradigm by identifying NAPEs as endogenous modulators of this axis. NAPE
253 accumulation attenuates PFF-induced LRRK2 upregulation and enhances α-synuclein clearance
254 in neuronal cells, whereas NAPE-PLD overexpression exacerbates both phenotypes. Importantly,
255 in human iPSC-derived dopaminergic neurons carrying the G2019S mutation, NAPE-PLD inhibition
256 restores lysosomal activity and reduces aggregate burden to levels comparable to isogenic
257 controls. These findings integrate LRRK2 hyperactivation and α-synuclein pathology into a unified
258 lipid-sensitive framework and suggest that modulation of NAPE metabolism can normalize
259 lysosomal function even in a genetically sensitized context.

260 From a therapeutic perspective, NAPE-PLD inhibition emerges as a promising strategy to restore
261 lysosomal proteostasis. By increasing endogenous NAPE levels, this approach enhances
262 lysosomal function and promotes α-synuclein clearance while potentially avoiding some of the
263 limitations associated with direct LRRK2 kinase inhibition. Small-molecule NAPE-PLD inhibitors
264 effectively elevate NAPEs without compensatory increases in FAEs (51), supporting their utility as
265 pharmacological tools. At the same time, given the broader roles of NAPEs and FAEs in brain
266 physiology, including regulation of feeding, reward, and anxiety (57, 58), careful in vivo studies will
267 be required to define therapeutic windows and assess long-term effects. Nonetheless, targeting a
268 stress-responsive lipid pathway offers a conceptually distinct and potentially complementary
269 strategy to address convergent lysosomal defects observed in both genetic and sporadic PD (56).

270 While our study provides a robust framework for NAPE-mediated regulation of LRRK2 and
271 lysosomal function, the study has some limitations. First, most mechanistic experiments were
272 performed in SH-SY5Y-derived neuronal cells, which only partially recapitulate mature nigral
273 dopaminergic neuron biology. The rescue of lysosomal activity and α-synuclein handling in human
274 G2019S dopaminergic neurons argues for disease relevance, but confirmation in in vivo (e.g.,
275 G2019S knock-in mice or α-synuclein PFF–injected rodents) will be important. Second, we focused
276 on cathepsin B activity and aggregate counts; future studies should expand to broader lysosomal
277 hydrolases, lysosomal pH, and TFEB/MiT–TFE transcriptional programs modulated by LRRK2 (36,
278 59). Finally, the molecular interface between NAPEs and LRRK2 remains to be defined; which
279 NAPE species are responsible, whether NAPEs alter Rab/scaffold recruitment (35, 48, 50), and
280 how NAPE dynamics interact with other lipid pathways, including glucocerebrosidase-dependent
281 sphingolipid metabolism. Addressing these questions will clarify how a stress-inducible membrane
282 lipid precisely controls a disease-critical kinase and may reveal new opportunities to fine-tune
283 lysosomal function in neurodegeneration.

284

285 **Materials and Methods**

286

287 ***Chemicals***

288 MLi-2 LRRK2 inhibitor was purchased from Selleckchem (S9694). Bafilomycin A1 was purchased
289 by Sigma-Aldrich (SML1661). Lei-401 NAPE-PLD inhibitor was kindly donated by Professor Van

290 der Stelt (Leiden University), DOPE-N-Nonadecanoyl standard was purchased by Larodan (38-
291 9091). Ionomycin was purchased by Sigma-Aldrich (I3909).

292 ***Culture of Cell lines and treatments***

293 Human neuroblastoma cell line SH-SY5Y (SK-N-SH-derived, hereafter "neuronal cells") were
294 cultured in RPMI1640 media (Euroclone, ECB2000L) and supplemented with 10% fetal calf serum
295 (FCS) (Eurobio Scientific, CVFSVF00-01) and 1% penicillin-streptomycin (PS, Gibco, 15140-122;
296 100 units/mL final concentration). Cells were maintained at 37°C in a humidified CO^2 incubator,
297 and passaged using 0.05% Trypsin-EDTA (Gibco, 25300-054) when they reached 90% confluence.
298 Cells were counted before each experiment, and seeded on autoclaved, 12 mm glass coverslips
299 (uncoated) (Epredia, CB00120RA120MNZ0) for fixed-cell imaging, or on 35 mm glass-bottom
300 microdishes (Ibidi GmbH, 80807-90) for live-cell imaging. Cells between passages 3 and 10 were
301 used for experiments. MLi-2 LRRK2 inhibitor (Selleckchem) was dissolved in DMSO and diluted in
302 full growth media to a final concentration of 10nM and incubated over-night. Bafilomycin A1 (Sigma-
303 Aldrich, 500X) was dissolved in fresh full growth media and incubated for 4h prior to further analysis.
304 LEI-401 was dissolved in in DMSO and diluted in full growth media to a final concentration of 1 μM
305 and incubated over-night. Ionomycin was diluted in full growth media to a final concentration of 5
306 μM and incubated 30 minutes.

307 ***Generation of NAPE-PLD knock-down cell lines***

308 The NAPE-PLD Human Gene Knockout Kit (CRISPR, Origene, KN409877) was used following
309 manufacturer's instructions. Lipofectamine™ 3000 Transfection Reagent (Thermo Fisher Scientific,
310 L3000001) was used following standard protocol in OptiMEM media supplemented with 1% PS and
311 1% FCS. One day before transfection, SH-SY5Y cells were seeded in a six-well plate to reach 80-
312 90% confluence at the time of transfection. Before transfection, culture medium was aspirated and
313 1715 µL of transfection medium was added. A mixture of donor DNA (10 µL per well), gRNA (20 µL
314 per well), P3000 reagent (2 µL per well), and Lipofectamine 3000 (3 µL per well) was prepared in
315 transfection medium (250 µl each) and incubated (15 min, room temperature). Transfection was
316 performed by dropwise addition of the transfection mixture to the cells. Then, 6 h post-transfection,
317 the culture medium was replenished with full growth media for additional 48 h. Cells were selected
318 in the medium containing 1 µg/mL puromycin. Clonal cell lines were selected by clonal dilution.
319 Three clones were used throughout this study.

320 ***Generation of PLA2G4E-overexpressing cell lines***

321 The pcDNA5/TO vector harboring EGFP-FL-PL2G4E was kindly donated by Professor Uyama
322 (Kagawa University, (33)) and transfected into SH-SY5Y cells using 5 µg of DNA per well and
323 Lipofectamine 3000 in OptiMEM media for 6h as described above. After 48 h from transfection,
324 cells were selected with the medium containing 500 µg/mL Geneticin (Gibco, 10131-027). Clonal
325 cell lines were generated by clonal dilution and maintained in the medium containing geneticin.
326 Three of the clones expressing EGF-PLA2G4E were used throughout this study.

327 ***Generation of NAPE-PLD-overexpressing cells***

328 Lentiviral particles were produced by transient transfection of HEK293T cells using
329 polyethyleneimine (PEI) (Sigma, #306185). Cells were seeded in 12-well plates at a density of 1.7
330 × 10^5 cells per well and incubated for 24 hours to reach 70–80% confluency. Transfection mixtures

were prepared in DMEM without FBS: the DNA mix contained 400 ng psPAX2 packaging plasmid (Addgene #12260), 350 ng VSV-G pseudotyping plasmid (Addgene #14888), 300 ng pRSV-Rev plasmid (Addgene #12253), and 650 ng NAPE-PLD-pLenti-C-mGFP-P2A-Puro transfer plasmid (OriGene #PS100093) (Fig. 1). A second mixture contained PEI diluted 1:50 in DMEM without FBS. The two mixtures were combined at a 1:1 ratio, vortexed gently, and incubated at room temperature for 20 minutes to allow PEI–DNA complex formation. Cell culture medium was replaced with fresh complete medium (DMEM + 10% FBS), and the transfection mixture was added dropwise to each well (total volume 100 µL per well). Cells were incubated at 37°C, 5% CO_2 for 48 hours. Supernatants were then harvested, centrifuged at 3,000 rpm (1,100 × g) for 15 minutes at 4°C to remove cellular debris, and the clarified lentiviral particle-containing supernatant was aliquoted, snap-frozen in liquid nitrogen, and stored at −80°C. Viral titers were not formally quantified but estimated as sufficient for downstream transduction based on pilot GFP expression assays.

Stable SH-SY5Y NAPE-PLD-overexpressing cells were generated by transduction with the harvested lentiviral supernatant. SH-SY5Y cells were seeded in 12-well plates at 2×10^5 cells per well and incubated for 24 hours. Medium was replaced with lentiviral supernatant supplemented with polybrene (Sigma, #H9268; final 8 µg/mL, 1:100 dilution from 0.8 mg/mL stock). Plates underwent spinoculation at 1,100 × g for 1 hour at 37°C to enhance transduction efficiency. Following spinoculation, plates were incubated for an additional 2 hours at 37°C, after which the medium was replaced with fresh DMEM/F-12 (1:1) supplemented with 2% FBS. Cells were recovered for 72 hours before initiating selection. Puromycin selection was performed in two sequential rounds: first at 5 µg/mL for 5 days, followed by 10 µg/mL for 7 days, with medium changes every 2–3 days. Transduction efficiency and selection success were confirmed by visualizing GFP fluorescence under a fluorescence microscope (Operetta CLS, Revvity, Milan). Selected polyclonal populations exhibited >95% GFP positivity and were expanded for downstream experiments.

Cell culture experiments with hiPSC lines

Dopaminergic neurons were generated from neural progenitor cells (NPCs) according to an established protocol (60). Briefly, NPCs at 80% confluency were dissociated using Accutase for 5 minutes at 37 °C and collected via centrifugation (1100 rpm, 5 min). Cells were then seeded onto matrigel-coated 6-well plates (1:10 dilution in DMEM/F12) at a density of 1.0×10^6 cells/well. Differentiation was initiated at day 0 by transitioning to differentiation medium. On day 6, the cells were passaged and re-seeded at 3.0×10^6 cells/well. Neuronal maturation began on day 8 with the addition of 0.5 µM PMA, which was subsequently withdrawn on day 10. On day 14, the dopaminergic neurons were harvested and re-plated at a density of 2.6×10^4 cells/cm, according to the experimental design planned. On day 21, cells were treated overnight with 1 µM LEI-401 and subsequently tested with magic red assay. Cells were treated with α-syn PFFs in the presence of vehicle or 1μM LEI-401 for 48 h, followed by fixation and immunofluorescence analysis.

Preparation of α-syn aggregates

α-Syn aggregates were prepared as described before (61). Briefly, human wild-type α-syn was purified from *Escherichia coli* BL21 (DE3) with RP-HPLC. Fibrils were then conjugated with Alexa Fluor™ 647 fluorophore (used in imaging experiments) (Invitrogen) using manufacturer's labelling kit or not tagged with a fluorophore. Fibrils were kept at -80°C for long-term storage. Prior to exposure to cells, fibrils were diluted in growth medium at a working concentration of 500 nM and

374 sonicated (BioBlock Scientific, Vibra Cell 7504) for 5 minutes at an amplitude of 80%, pulsed for 5
375 seconds “on” and 2 seconds “off”. Sonicated fibrils were then added on cells directly without the
376 addition of any intracellular delivery agents for designated time points.

377 ***Immunocytochemistry***

378 Immunofluorescence on cells were performed using the standard protocol. Cells were fixed with
379 4% paraformaldehyde (PFA [Electron Microscopy Sciences, 15710]) for 20 minutes at room
380 temperature (RT), followed by three washes with 1X DPBS. Cells were incubated in 1X DPBS-Tx
381 (0.1% Triton-X100 [Sigma Aldrich, 9002-93-1] in 1X DPBS) for 3 minutes at RT, followed by
382 incubation with blocking solution of 2% bovine serum albumin (BSA [Sigma Aldrich, A9647])
383 prepared in 1X DPBS for 1h at RT. Cells were then incubated with primary antibody overnight at
384 4°C. The following primary antibodies were used: rabbit anti-NAPE-PLD (Sigma Aldrich,
385 HPA024338, 1:200), rabbit anti-PLA2G4E (Proteintech, 18088-1-AP, 1:400), rabbit anti-LRRK2
386 (Abcam, ab133474; 1:500) mouse anti-LAMP1 (Developmental Studies Hybridoma Bank, H4A3;
387 1:100), guinea pig anti-p62 (Progen, GP62-C; 1:500), rabbit anti-TFEB (Cell Signaling Technology,
388 4240; 1:100), chicken anti-MAP2 (BioLegend, 82250, 1:10,000), rabbit anti-TH (Pel-Freez, P40101,
389 1:1,000), and mouse anti-βIII-tubulin (BioLegend, 801202, 1:1,000). The next day, cells were
390 washed three times with DPBS, followed by incubation with respective secondary antibodies (all
391 from Thermo fisher Scientific, dilution of 1:500 in blocking solution) for 1h at RT. Cells were then
392 washed three times with 1X DPBS, counterstained for nuclei with DAPI (1:1000 in PBS [Sigma-
393 Aldrich, D9542]) and mounted on glass slides with Aqua-Poly/Mount (Polysciences Inc., 18606-
394 20). Slides were imaged at least a day after mounting of coverslips.

395 ***Magic red CTSB assay***

396 Intracellular CTSB activity was measured in SH-SY5Y cells and dopaminergic iNeurons using the
397 Magic Red™ CTSB assay kit from Abcam, ab270772, according to the manufacturer’s protocol.
398 Cells were plated in glass-bottom matteks (Ibidi GmbH, 80807-90) the day before the experiment
399 to reach a 70-80% confluence for neuronal cells, or two weeks before for iNeurons. Culture medium
400 was gently removed and replaced with pre-warmed medium containing Magic Red substrate and
401 Hoechst 33342 (Abcam, AB270772, 1:100). Ionomycin was diluted in the same media containing
402 Magic Red to a final concentration of 1μM. Cells were incubated at 37 °C, 5% CO_2 for 30 min,
403 protected from light. Following incubation, media was replaced with Phenol-free media and
404 immediately live-imaged using a Nikon Eclipse Ti2 microscope with a spinning disk confocal set-
405 up (Yokogawa) equipped with a live-cell incubation chamber that maintained the samples at 37 °C
406 in a humidified atmosphere of 5% CO_2 throughout imaging. Cells were imaged using a 100X oil
407 immersion objective (1.45 numerical aperture). Optical sections of 0.5 μm interval were taken to
408 acquire the whole volume of the cells. Exposure time and gain were kept constant across all
409 experimental conditions within each experiment.

410 ***Immunoblotting***

411 Cell pellets were homogenized in 100 µl of radioimmunoprecipitation assay (RIPA) buffer consisting
412 of 50 mM Tris-HCl (pH 7.4), 1% TritonX-100, 0.5% sodium-deoxycholate, 0.1% sodium dodecyl
413 sulphate, 150 mM sodium chloride and 2 mM ethylenediaminetetraacetic acid, supplemented with
414 1X protease inhibitor (cOmplete Mini, EDTA-free; Sigma, 11836170001). Protein concentrations
415 were measured using Bradford’s method, following manufacturer’s instructions (Thermo Fisher
416 Scientific). Proteins (20 µg) were denatured in SDS (8%) and β-mercaptoethanol (5%) at 95 °C for

417 10 minutes. After separation by SDS-PAGE on a 4-20% gel (Biorad, 4568094), proteins were
418 electro-transferred to nitrocellulose membranes. The membranes were blocked with Tropix I-Block
419 buffer (Applied Biosystems, Thermo Fisher Scientific, T2015) and incubated overnight with primary
420 antibodies (anti-NAPE-PLD, Sigma-Aldrich, HPA024338, 1:500; anti-PLA2G4E, Proteintech,
421 18088-1-AP, 1:1000; anti Rab8a, Abcam, Ab188574, 1:500; anti-pT72Rab8a, Abcam, Ab230260,
422 1:1000; anti-GAPDH antibody Sigma-Aldrich, G9545, 1:5000; anti-Actin, MP Biomedicals, 691001,
423 1:1000) in blocking buffer, followed by incubation with horseradish peroxidase-conjugated
424 secondary antibody (Millipore, 1:5000) in TBS containing 0.1% Tween-20 at room temperature for
425 1 h. Finally, proteins were visualized using an ECL kit (Thermo Fisher Scientific, 34580) and
426 chemiluminescence images were acquired using GE Amersham Imager AI680 analyzer.

427 ***mRNA isolation and qPCR***

428 Total RNA was prepared from cell pellets using the Ambion PureLink RNA minikit (Invitrogen,
429 Thermo Fisher Scientific, 12183018A) as directed by the supplier. Samples were treated with
430 DNase (PureLink DNase, Invitrogen, Thermo Fisher Scientific, 12185010) and cDNA synthesis was
431 carried out using the high-capacity cDNA reverse transcription kit (Applied Biosystems, Thermo
432 Fisher Scientific 4368814) according to the manufacturer's protocol using purified RNA (0.5-1 µg).
433 First-strand cDNA was amplified using the iTaq universal SYBR Green supermix (Bio-Rad,
434 1725124). Copy numbers of cDNA targets were quantified at the cycle threshold. Quantitative PCR
435 was performed in 384-well PCR plates and run at 95°C for 10 min, followed by 40 cycles, each
436 cycle consisting of 15 s at 95°C and 1 min at 60°C, using a CFX 384-Real Time System (Bio-Rad).
437 The BestKeeper software (62) was used to determine expression stability and geometric mean of
438 three different housekeeping genes (Actin, GAPDH and HPRT). ΔCt values were calculated by
439 subtracting the Ct value of the geometric mean of these housekeeping genes from the Ct value for
440 the genes of interest. The relative quantity of genes of interest was calculated by the expression
441 $2^{-\Delta\Delta Ct}$. Results are reported as fold induction over control.

442 ***Lipid extraction and LC/MS analyses***

443 NAPE levels were measured as previously described (29). Briefly, snap-frozen cell pellets were
444 homogenized in a chloroform:methanol mixture (1:2 v/v, 2 mL) containing DOPE-N-Nonadecanoyl
445 (Larodan, #38-9091) as internal standards. Lipids were extracted twice with chloroform (0.6 mL)
446 and the organic phases were washed with water (0.6 mL), collected, and dried under nitrogen
447 stream. The organic extracts from cells were reconstituted in a mix of methanol/chloroform (9:1 v/v,
448 0.1 mL). Targeted analysis of the samples was carried out on a Waters Acquity UPLC system
449 coupled with a Xevo TQ-MS triple quadrupole mass spectrometer. NAPEs were separated on a
450 reversed-phase BEH C18 column (2.1 x 50 mm, 1.7 µm), whose temperature was kept at 55°C,
451 and eluted at a flow rate of 0.450 mL/min using the following gradient conditions: A = 10 mM
452 ammonium formate in acetonitrile/water (60:40 v/v), B = 10 mM ammonium formate in isopropyl
453 alcohol/acetonitrile (90:10 v/v); 0.0-1.0 min 40% B, 1.0-7.0 min 40 to 100% B, 7.0-8.0 min at 100%
454 B. The column was then reconditioned at 40% B for 1 min. The total run time was 9 min and the
455 injection volume was set to 5 µL. The mass spectrometer operated in the positive ESI mode and
456 analytes were quantified by multiple reaction monitoring (MRM), following the transitions reported
457 in Table 2. The capillary and the cone voltages were set at 3 kV and 30 V for all transitions,
458 respectively. The source temperature was set to 120 °C. Desolvation and cone gas flows (N_2) were
459 set to 800 and 50 l/h, respectively. Desolvation temperature was set at 450°C. Data were acquired
460 by MassLynx software and quantified by TargetLynx software. Quantification of NAPE species was

461 performed by means of a six-point calibration curve where standards were prepared by spiking the
462 only non-endogenous synthetic NAPE reference analytical standard we could purchase, DOPE-N-
463 19 (18:1/18:1/N19:0) in matrix at six different concentrations, from 1 to 500 nM.

464 As this LC/MS-MS protocol does not allow one to differentiate sn-1 from sn-2 substituents,
465 individual NAPE species are designated below as NAPE (X:Y-N-acyl, **Table 2**), where X is the total
466 number of carbon atoms and Y the total number of double bonds in the sn-1 and sn-2 chains.

467 ***Fixed-cell microscopy***

468 Images were acquired using a Nikon Eclipse Ti2 microscope with a spinning disk confocal set-up
469 (Yokogawa) equipped with four lasers (wavelength in nm): 405, 488, 561 and 640 nm. Samples
470 were imaged using a 100X oil immersion objective (1.45 numerical aperture) with a 1x zoom. The
471 entire cell volume was imaged for all samples, with optical sections of 0.5 μm.

472 Super-resolution images were acquired using Zeiss LSM 780 Elyra SIM set-up (Carl Zeiss,
473 Germany) using Plan-Apochromat 63×/1.4 oil objective with a 1.518 refractive index oil (Carl Zeiss).
474 16-bit images were acquired in "frame-fast" mode between wavelengths, with 32.0 μm grid size.
475 Optical thickness was set at 0.133 μm. Raw images were processed using the SIM processing tool
476 of Zen black software.

477 ***Quantification and Statistical Analyses***

478 Images were processed for analysis using FIJI software (). Colocalization analysis was performed
479 using the JACoP plug-in FIJI (63). 3D images were used for colocalizing two channels with object-
480 based detection, and thresholding of objects was performed manually.

481 No prior power analysis was done to measure the sample size. Graphs were plotted using
482 GraphPad prism 10.0, and appropriate statistical tests were performed on raw data. For all
483 datasets, an initial normality distribution test was performed, and non-parametric tests were
484 performed for any datasets that did not satisfy normal distribution. Statistical tests performed are
485 mentioned in the figure legends. All the experiments were performed for three independent
486 biological replicates.

487

Acknowledgments

We are grateful to Prof. Toro Uyama and Prof. Natsuo Ueda for generously providing the EGFP-FL-PL2G4E construct, and to Prof. Mario van der Stelt for providing the NAPE-PLD inhibitor LEI-401. We thank Prof. Takashi Nonaka for providing the α-synuclein fibrils. We are grateful to Dr. Valeria Valente and Dr. Ranabir Chakraborty for critical reading of the manuscript; we also thank Dr. Ranabir Chakraborty for assistance with super-resolution image processing. We thank Dr. Audrey Salles for technical assistance with super-resolution microscopy. We also thank all members of the Membrane Traffic and Pathogenesis Unit at the Institut Pasteur for insightful discussions. Finally, we thank Reine Bouyssie, from the administrative staff of the Membrane Traffic and Pathogenesis Unit, for her continued support.

The present study was funded by MSCA-IF-Fellowship LipiSyn – 101064077 (FP) and Fondation Alzheimer Young Researcher Program, 990987 (FP), France Parkinson - Soutien de l'Association France Parkinson AAP 2021 (CZ), Don Explore AD - Programme Explore de l'Institut Pasteur (CZ), Agence Nationale de la Recherche ANR-20-CE13-0032-01 (CZ), ANR-23-CE16-0012-03 UnProSec (CZ), Fondation pour la Recherche Médicale FRM - EQU202103012692 (CZ), FRMMND202310017892 (CZ), Fondation Alzheimer AAP 2024 (CZ).

References

1. D. Coulon, L. Faure, M. Salmon, V. Wattelet, J.-J. Bessoule, Occurrence, biosynthesis and functions of N-acylphosphatidylethanolamines (NAPE): not just precursors of N-acylethanolamines (NAE). *Biochimie* **94**, 75–85 (2012).

2. J. Liu, *et al.*, A biosynthetic pathway for anandamide. *Proc. Natl. Acad. Sci. U. S. A.* **103**, 13345–13350 (2006).

3. S. M. K. Rahman, *et al.*, Formation of N-acyl-phosphatidylethanolamines by cytosolic phospholipase A2ε in an ex vivo murine model of brain ischemia. *Biochim. Biophys. Acta Mol. Cell Biol. Lipids* **1867**, 159222 (2022).

4. Y. Ogura, W. H. Parsons, S. S. Kamat, B. F. Cravatt, A calcium-dependent acyltransferase that produces N-acyl phosphatidylethanolamines. *Nat. Chem. Biol.* **12**, 669–671 (2016).

5. Y. Okamoto, J. Morishita, K. Tsuboi, T. Tonai, N. Ueda, Molecular characterization of a phospholipase D generating anandamide and its congeners. *J. Biol. Chem.* **279**, 5298–5305 (2004).

6. P. Magotti, *et al.*, Structure of human N-acylphosphatidylethanolamine-hydrolyzing phospholipase D: regulation of fatty acid ethanolamide biosynthesis by bile acids. *Structure* **23**, 598–604 (2015).

7. H. Cadas, E. di Tomaso, D. Piomelli, Occurrence and biosynthesis of endogenous cannabinoid precursor, N-arachidonoyl phosphatidylethanolamine, in rat brain. *J. Neurosci. Off. J. Soc. Neurosci.* **17**, 1226–1242 (1997).

527 8. T. Zimmermann, *et al.*, Impaired anandamide/palmitoylethanolamide signaling in
528 hippocampal glutamatergic neurons alters synaptic plasticity, learning, and emotional
529 responses. *Neuropsychopharmacol. Off. Publ. Am. Coll. Neuropsychopharmacol.* **44**, 1377–
530 1388 (2019).

531 9. J. M. Walker, S. M. Huang, N. M. Strangman, K. Tsou, M. C. Sañudo-Peña, Pain modulation
532 by release of the endogenous cannabinoid anandamide. *Proc. Natl. Acad. Sci. U. S. A.* **96**,
533 12198–12203 (1999).

534 10. M. Igarashi, *et al.*, Dietary oleic acid contributes to the regulation of food intake through
535 the synthesis of intestinal oleoylethanolamide. *Front. Endocrinol.* **13**, 1056116 (2022).

536 11. N. V. DiPatrizio, D. Piomelli, Intestinal lipid-derived signals that sense dietary fat. *J. Clin.*
537 *Invest.* **125**, 891–898 (2015).

538 12. S. D. Skaper, *et al.*, N-Palmitoylethanolamine and Neuroinflammation: a Novel Therapeutic
539 Strategy of Resolution. *Mol. Neurobiol.* **52**, 1034–1042 (2015).

540 13. J. Lo Verme, *et al.*, The nuclear receptor peroxisome proliferator-activated receptor-alpha
541 mediates the anti-inflammatory actions of palmitoylethanolamide. *Mol. Pharmacol.* **67**,
542 15–19 (2005).

543 14. M. P. Gillum, *et al.*, N-acylphosphatidylethanolamine, a gut- derived circulating factor
544 induced by fat ingestion, inhibits food intake. *Cell* **135**, 813–824 (2008).

545 15. C. Janfelt, *et al.*, Visualization by mass spectrometry of 2-dimensional changes in rat brain
546 lipids, including N-acylphosphatidylethanolamines, during neonatal brain ischemia. *FASEB*
547 *J. Off. Publ. Fed. Am. Soc. Exp. Biol.* **26**, 2667–2673 (2012).

548 16. V. Natarajan, P. C. Schmid, H. H. Schmid, N-acylethanolamine phospholipid metabolism in
549 normal and ischemic rat brain. *Biochim. Biophys. Acta* **878**, 32–41 (1986).

550 17. D. Luptakova, *et al.*, Membrane depolarization and aberrant lipid distributions in the
551 neonatal rat brain following hypoxic-ischaemic insult. *Sci. Rep.* **8**, 6952 (2018).

552 18. H. H. Hansen, C. Ikonomidou, P. Bittigau, S. H. Hansen, H. S. Hansen, Accumulation of the
553 anandamide precursor and other N-acylethanolamine phospholipids in infant rat models
554 of in vivo necrotic and apoptotic neuronal death. *J. Neurochem.* **76**, 39–46 (2001).

555 19. H. S. Hansen, *et al.*, Characterization of glutamate-induced formation of N-
556 acylphosphatidylethanolamine and N-acylethanolamine in cultured neocortical neurons. *J.*
557 *Neurochem.* **69**, 753–761 (1997).

558 20. M. Saito, *et al.*, Ethanol alters lipid profiles and phosphorylation status of AMP-activated
559 protein kinase in the neonatal mouse brain. *J. Neurochem.* **103**, 1208–1218 (2007).

560 21. A. Basit, S. Pontis, D. Piomelli, A. Armirotti, Ion mobility mass spectrometry enhances low-
561 abundance species detection in untargeted lipidomics. *Metabolomics Off. J. Metabolomic*
562 *Soc.* **12**, 50 (2016).

563 22. H. H. Hansen, S. H. Hansen, A. Schousboe, H. S. Hansen, Determination of the phospholipid
564 precursor of anandamide and other N-acylethanolamine phospholipids before and after
565 sodium azide-induced toxicity in cultured neocortical neurons. *J. Neurochem.* **75**, 861–871
566 (2000).

567 23. M. J. Swamy, P. K. Tarafdar, R. K. Kamlekar, Structure, phase behaviour and membrane
568 interactions of N-acylethanolamines and N-acylphosphatidylethanolamines. *Chem. Phys.*
569 *Lipids* **163**, 266–279 (2010).

570 24. C. P. Lafrance, J. E. Blochet, M. Pézolet, N-acylphosphatidylethanolamines: effect of the N-
571 acyl chain length on its orientation. *Biophys. J.* **72**, 2559–2568 (1997).

572 25. T. Shangguan, C. C. Pak, S. Ali, A. S. Janoff, P. Meers, Cation-dependent fusogenicity of an
573 N-acyl phosphatidylethanolamine. *Biochim. Biophys. Acta* **1368**, 171–183 (1998).

574 26. X.-M. Li, M. Ramakrishnan, H. L. Brockman, R. E. Brown, M. J. Swamy, N-Myristoylated
575 Phosphatidylethanolamine: Interfacial Behavior and Interaction with Cholesterol.
576 *Langmuir ACS J. Surf. Colloids* **18**, 231–238 (2002).

577 27. D.-C. Chiu, Y.-T. Cho, H. Lin, J. M. Baskin, Photoaffinity Labeling Reveals a Role for the
578 Unusual Triply Acylated Phospholipid N-Acylphosphatidylethanolamine in Lactate
579 Homeostasis. *J. Am. Chem. Soc.* **147**, 33386–33394 (2025).

580 28. F. Palese, S. Pontis, N. Realini, D. Piomelli, NAPE-specific phospholipase D regulates LRRK2
581 association with neuronal membranes. *Adv. Pharmacol.* **90**, 217–238 (2021).

582 29. F. Palese, S. Pontis, N. Realini, D. Piomelli, A protective role for N-
583 acylphosphatidylethanolamine phospholipase D in 6-OHDA-induced neurodegeneration.
584 *Sci. Rep.* **9**, 15927 (2019).

585 30. Z. Hamid, *et al.*, Gender specific decrease of a set of circulating N-acylphosphatidyl
586 ethanolamines (NAPEs) in the plasma of Parkinson's disease patients. *Metabolomics Off. J.*
587 *Metabolomic Soc.* **15**, 74 (2019).

588 31. H. M. Bailey, M. R. Cookson, How Parkinson's Disease-Linked LRRK2 Mutations Affect
589 Different CNS Cell Types. *J. Park. Dis.* **14**, 1331–1352 (2024).

590 32. C. Klein, A. Westenberger, Genetics of Parkinson's disease. *Cold Spring Harb. Perspect.*
591 *Med.* **2**, a008888 (2012).

592 33. S. S. Binte Mustafiz, *et al.*, The role of intracellular anionic phospholipids in the production
593 of N-acyl-phosphatidylethanolamines by cytosolic phospholipase A2ε. *J. Biochem. (Tokyo)*
594 **165**, 343–352 (2019).

595 34. E. Kania, *et al.*, LRRK2 phosphorylation status and kinase activity regulate
596 (macro)autophagy in a Rab8a/Rab10-dependent manner. *Cell Death Dis.* **14**, 436 (2023).

597 35. T. Eguchi, *et al.*, LRRK2 and its substrate Rab GTPases are sequentially targeted onto
598 stressed lysosomes and maintain their homeostasis. *Proc. Natl. Acad. Sci. U. S. A.* **115**,
599 E9115–E9124 (2018).

600 36. N. Yadavalli, S. M. Ferguson, LRRK2 suppresses lysosome degradative activity in
601 macrophages and microglia through MiT-TFE transcription factor inhibition. *Proc. Natl.*
602 *Acad. Sci. U. S. A.* **120**, e2303789120 (2023).

603 37. M. Madureira, N. Connor-Robson, R. Wade-Martins, LRRK2: Autophagy and Lysosomal
604 Activity. *Front. Neurosci.* **14**, 498 (2020).

605 38. J. Obergasteiger, *et al.*, Kinase inhibition of G2019S-LRRK2 enhances autolysosome
606 formation and function to reduce endogenous alpha-synuclein intracellular inclusions. *Cell*
607 *Death Discov.* **6**, 45 (2020).

608 39. S. S. Binte Mustafiz, *et al.*, Intracellular Ca2+-dependent formation of N-acyl-
609 phosphatidylethanolamines by human cytosolic phospholipase A2ε. *Biochim. Biophys. Acta*
610 *Mol. Cell Biol. Lipids* **1864**, 158515 (2019).

611 40. M. Palmieri, *et al.*, Characterization of the CLEAR network reveals an integrated control of
612 cellular clearance pathways. *Hum. Mol. Genet.* **20**, 3852–3866 (2011).

613 41. S. MacIsaac, *et al.*, Neuron-autonomous susceptibility to induced synuclein aggregation is
614 exacerbated by endogenous Lrrk2 mutations and ameliorated by Lrrk2 genetic knock-out.
615 *Brain Commun.* **2**, fcz052 (2020).

616 42. E.-J. Bae, *et al.*, LRRK2 kinase regulates α-synuclein propagation via RAB35
617 phosphorylation. *Nat. Commun.* **9**, 3465 (2018).

618 43. Y. Okamoto, *et al.*, Mammalian cells stably overexpressing N-
619 acylphosphatidylethanolamine-hydrolysing phospholipase D exhibit significantly decreased
620 levels of N-acylphosphatidylethanolamines. *Biochem. J.* **389**, 241–247 (2005).

621 44. K. Ahn, *et al.*, Discovery and characterization of a highly selective FAAH inhibitor that
622 reduces inflammatory pain. *Chem. Biol.* **16**, 411–420 (2009).

623 45. R. Wallings, N. Connor-Robson, R. Wade-Martins, LRRK2 interacts with the vacuolar-type
624 H+-ATPase pump a1 subunit to regulate lysosomal function. *Hum. Mol. Genet.* **28**, 2696–
625 2710 (2019).

626 46. A. B. West, *et al.*, Parkinson's disease-associated mutations in leucine-rich repeat kinase 2
627 augment kinase activity. *Proc. Natl. Acad. Sci. U. S. A.* **102**, 16842–16847 (2005).

628 47. J. Schapansky, *et al.*, Familial knockin mutation of LRRK2 causes lysosomal dysfunction and
629 accumulation of endogenous insoluble α-synuclein in neurons. *Neurobiol. Dis.* **111**, 26–35
630 (2018).

631 48. J. H. Kluss, *et al.*, Lysosomal positioning regulates Rab10 phosphorylation at LRRK2+
632 lysosomes. *Proc. Natl. Acad. Sci. U. S. A.* **119**, e2205492119 (2022).

633 49. L. Bonet-Ponce, *et al.*, LRRK2 mediates tubulation and vesicle sorting from lysosomes. *Sci.*
634 *Adv.* **6**, eabb2454 (2020).

635 50. X. Wang, *et al.*, Rab12 is a regulator of LRRK2 and its activation by damaged lysosomes.
636 *eLife* **12**, e87255 (2023).

637 51. B. Castellani, *et al.*, Synthesis and characterization of the first inhibitor of N-
638 acylphosphatidylethanolamine phospholipase D (NAPE-PLD). *Chem. Commun.* **53**, 12814–
639 12817 (2017).

640 52. P. Rivera, *et al.*, Localization of peroxisome proliferator-activated receptor alpha (PPARα)
641 and N-acyl phosphatidylethanolamine phospholipase D (NAPE-PLD) in cells expressing the
642 Ca(2+)-binding proteins calbindin, calretinin, and parvalbumin in the adult rat
643 hippocampus. *Front. Neuroanat.* **8**, 12 (2014).

644 53. S. Wójtowicz, A. K. Strosznajder, M. Jeżyna, J. B. Strosznajder, The Novel Role of PPAR
645 Alpha in the Brain: Promising Target in Therapy of Alzheimer's Disease and Other
646 Neurodegenerative Disorders. *Neurochem. Res.* **45**, 972–988 (2020).

647 54. Y. S. Kim, *et al.*, PPAR-α Activation Mediates Innate Host Defense through Induction of
648 TFEB and Lipid Catabolism. *J. Immunol.* **198**, 3283–3295 (2017).

649 55. P. Holland, *et al.*, HS1BP3 negatively regulates autophagy by modulation of phosphatidic
650 acid levels. *Nat. Commun.* **7**, 13889 (2016).

651 56. A. Sanyal, H. S. Novis, E. Gasser, S. Lin, M. J. LaVoie, LRRK2 Kinase Inhibition Rescues
652 Deficits in Lysosome Function Due to Heterozygous GBA1 Expression in Human iPSC-
653 Derived Neurons. *Front. Neurosci.* **14**, 442 (2020).

654 57. E. D. Mock, *et al.*, Discovery of a NAPE-PLD inhibitor that modulates emotional behavior in
655 mice. *Nat. Chem. Biol.* **16**, 667–675 (2020).

656 58. E. Leishman, K. Mackie, S. Luquet, H. B. Bradshaw, Lipidomics profile of a NAPE-PLD KO
657 mouse provides evidence of a broader role of this enzyme in lipid metabolism in the brain.
658 *Biochim. Biophys. Acta* **1861**, 491–500 (2016).

659 59. T. Kuwahara, T. Iwatsubo, The Emerging Functions of LRRK2 and Rab GTPases in the
660 Endolysosomal System. *Front. Neurosci.* **14**, 227 (2020).

661 60. P. Reinhardt, *et al.*, Derivation and expansion using only small molecules of human neural
662 progenitors for neurodegenerative disease modeling. *PloS One* **8**, e59252 (2013).

663 61. T. Nonaka, S. T. Watanabe, T. Iwatsubo, M. Hasegawa, Seeded aggregation and toxicity of
664 {alpha}-synuclein and tau: cellular models of neurodegenerative diseases. *J. Biol. Chem.*
665 **285**, 34885–34898 (2010).

666 62. M. W. Pfaffl, A. Tichopad, C. Prgomet, T. P. Neuvians, Determination of stable
667 housekeeping genes, differentially regulated target genes and sample integrity:
668 BestKeeper--Excel-based tool using pair-wise correlations. *Biotechnol. Lett.* **26**, 509–515
669 (2004).

670 63. S. Bolte, F. P. Cordelières, A guided tour into subcellular colocalization analysis in light
671 microscopy. *J. Microsc.* **224**, 213–232 (2006).

672

673

674 **Figures and Tables**

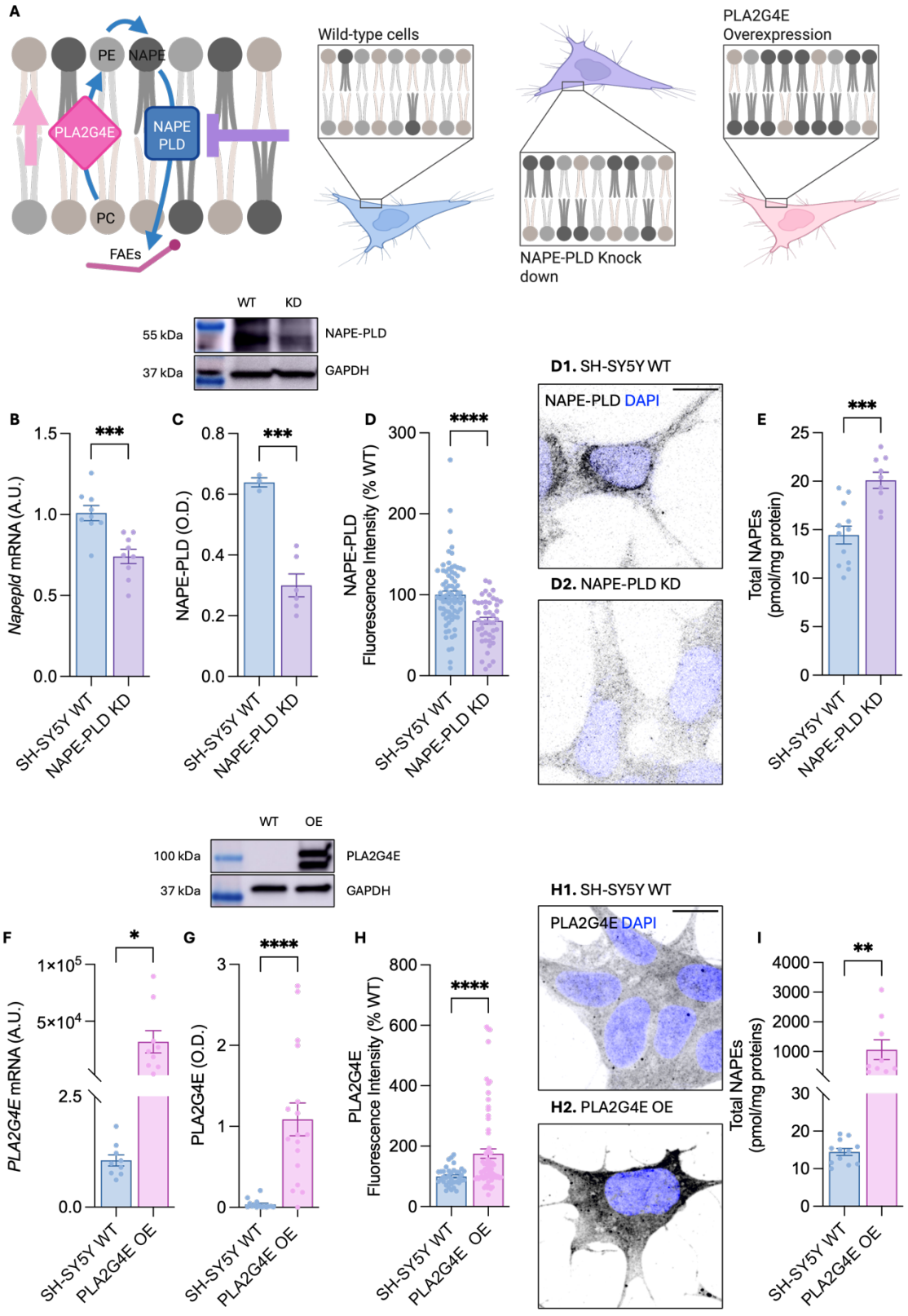

675

676 **Figure 1. Generation of catecholaminergic SH-SY5Y neuronal cells accumulating NAPEs.**
677 (**A**) Schematic representation of the experimental strategy. Stable SH-SY5Y cell lines were
678 generated either by knocking down NAPE-PLD using CRISP-Cas9 approach or by overexpressing
679 PLA2G4E, both manipulations led to NAPE accumulation at the cell membranes. (**B**) *NAPE-PLD*
680 mRNA levels in NAPE-PLD-knockdown (KD; violet bars) and wild-type (WT; blue bars) cells. (**C**)
681 Western blot analysis of NAPE-PLD protein levels in KD and WT cells. Top, representative blot;
682 bottom, densitometric quantification normalized to glyceraldehyde 3-phosphate dehydrogenase
683 (GAPDH). (**D**) Immunofluorescence analysis of NAPE-PLD (gray) with representative images (**D1,**
684 **D2**) and quantification. Nuclei were counterstained with DAPI. (**E**) Total NAPE levels in KD and WT
685 cells. (**F**) *PLA2G4E* mRNA levels in PLA2G4E-overexpressing (OE; pink bars) and WT (blue bars)
686 cells. (**G**) Western blot analysis of PLA2G4E protein levels in OE and WT cells. Top, representative
687 blot; bottom, densitometric quantification normalized to GAPDH. (**H**) Immunofluorescence analysis
688 of PLA2G4E (gray) with representative images (**H1, H2**) and quantification. Nuclei were
689 counterstained with DAPI. (**I**) Total NAPE levels in OE and WT cells. Error bars represent SEM. *P
690 < 0.05, **P < 0.01 ***P < 0.001, ****P < 0.0001 Student's *t*-test with Welch's correction. Scale bars,
691 10 μm.

692

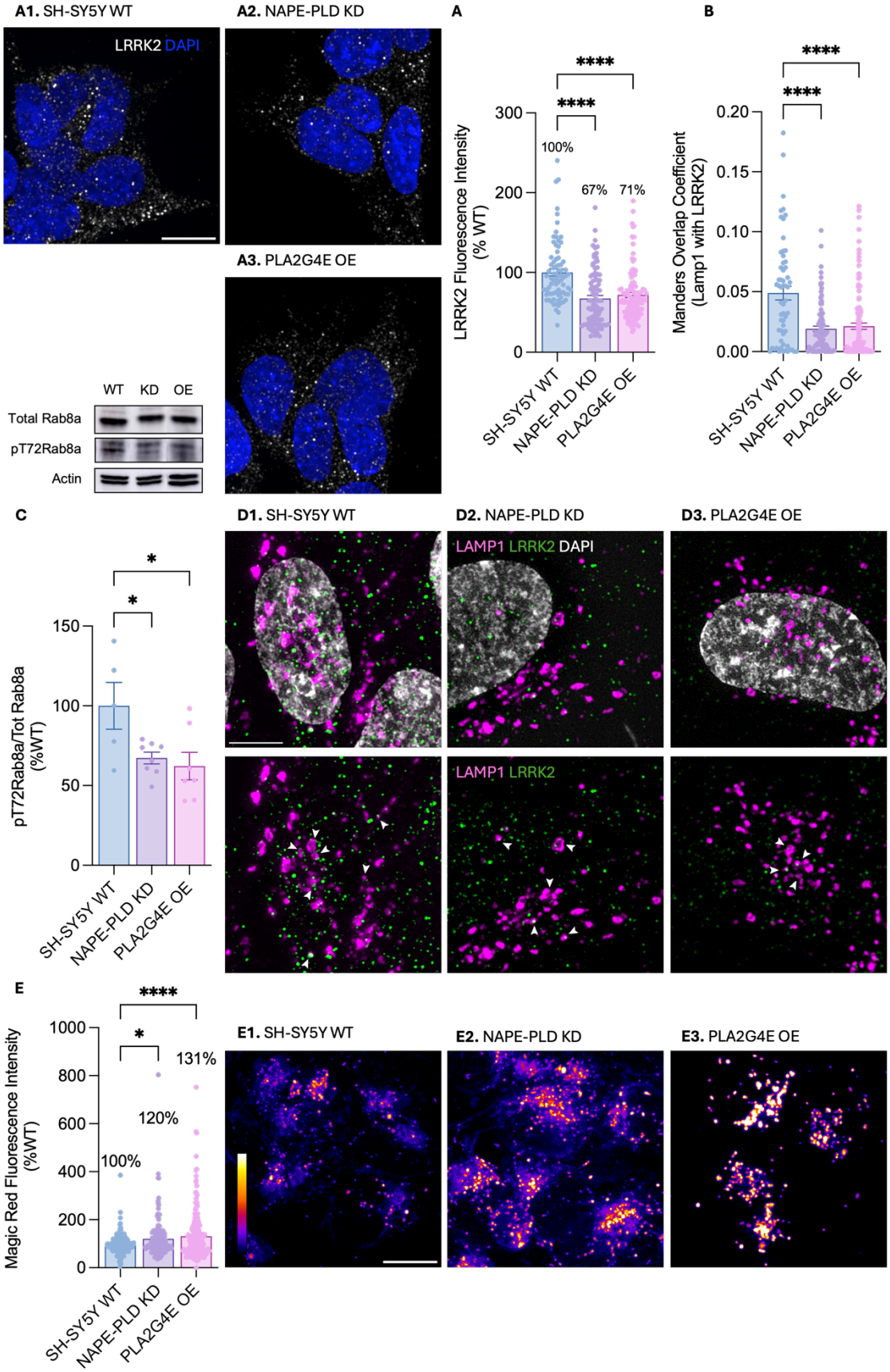
A1. SH-SY5Y WT
LRRK2 DAPI
A2. NAPE-PLD KD
A3. PLA2G4E OE
A
LRRK2 Fluorescence Intensity (% WT)
300
200
100
0
****
****
100%
67%
71%
SH-SY5Y WT
NAPE-PLD KD
PLA2G4E OE
B
Manders Overlap Coefficient (Lamp1 with LRRK2)
0.20
0.15
0.10
0.05
0.00
****
****
SH-SY5Y WT
NAPE-PLD KD
PLA2G4E OE
WT KD OE
Total Rab8a
pT72Rab8a
Actin
C
pT72Rab8a/Tot Rab8a (%WT)
150
100
50
0
*
*
SH-SY5Y WT
NAPE-PLD KD
PLA2G4E OE
D1. SH-SY5Y WT
D2. NAPE-PLD KD
D3. PLA2G4E OE
LAMP1 LRRK2 DAPI
LAMP1 LRRK2
E
Magic Red Fluorescence Intensity (%WT)
1000
800
600
400
200
0
****
*
100%
120%
131%
SH-SY5Y WT
NAPE-PLD KD
PLA2G4E OE
E1. SH-SY5Y WT
E2. NAPE-PLD KD
E3. PLA2G4E OE

693

Figure 2. Neuronal cells accumulating NAPEs downregulate LRRK2 protein and potentiate lysosomal activity. (**A**) Immunofluorescence analysis of LRRK2 (gray) with representative images (**A1–A3**) and quantification in wild-type (WT; **A1**, blue), NAPE-PLD knockdown (KD; **A2**, violet), and PLA2G4E-overexpressing (OE; **A3**, pink) SH-SY5Y cells. Nuclei were counterstained with DAPI. (**B**) Quantification of the colocalization between LAMP1-positive structures and LRRK2, expressed as Manders' overlap coefficient for the fraction of LAMP1 signal overlapping with LRRK2. (**C**) Western blot analysis of Rab8a and phosphorylated Rab8a (pT72-Rab8a) in KD and OE compared with WT cells. Top, representative blot; bottom, densitometric quantification normalized to actin. (**D**) Representative super-resolution immunofluorescence images of LAMP1 (magenta) and LRRK2 (green) in WT (**D1**), NAPE-PLD KD (**D2**), and PLA2G4E OE (**D3**) cells. Nuclei were stained with DAPI (gray). Scale bar, 5 μm. (**E**) Fluorescence intensity quantification and representative images of the Magic Red–cathepsin B assay, indicating lysosomal degradative capacity per cell, in WT (**E1**), NAPE-PLD KD (**E2**), and PLA2G4E OE (**E3**) cells. Representative images are displayed using the FIRE lookup table (LUT) to indicate fluorescence intensity. Scale bars, 10 μm. Mean values are indicated in the graphs; error bars represent SEM. *P < 0.05, ****P < 0.0001; one-way ANOVA with Tukey's multiple-comparison test.

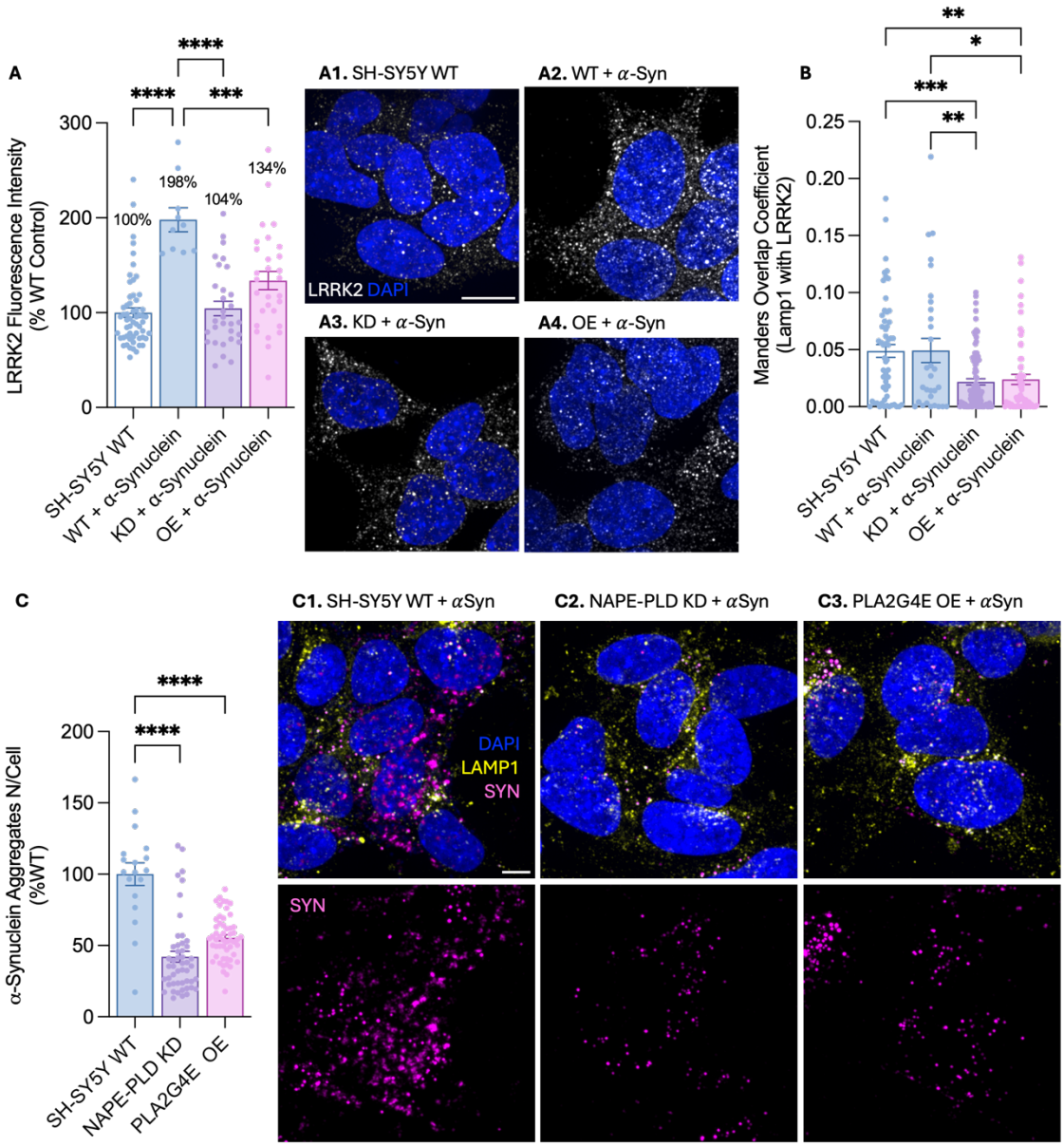

Figure 3. Neuronal cells accumulating NAPEs prevent LRRK2 accumulation following α-synuclein treatment and enhance aggregate clearance. (**A**) Immunofluorescence analysis of LRRK2 (gray) with representative images (**A1-A4**) and quantification in WT (**A1, A2**), NAPE-PLD-knockdown (KD; **A3**), and PLA2G4E-overexpressing (OE; **A4**) cells treated or not with α-syn (**A2-A4**). (**B**) Quantification of the colocalization between LAMP1-positive structures and LRRK2, expressed as Mander's overlap coefficient for the fraction of LAMP1 signal overlapping with LRRK2. (**C**) Quantification and representative images of α-syn aggregate number per cell in WT (**C1**), NAPE-PLD KD (**C2**) and PLA2G4E OE (**C3**) cells. LAMP1 is shown in yellow, α-syn in pink, and nuclei were counterstained with DAPI (blue). Scale bar, 10 μm. Mean values are indicated in the graphs; error bars represent SEM. ***P < 0.001, ****P < 0.0001; one-way ANOVA with Tuckey's multiple-comparison test.

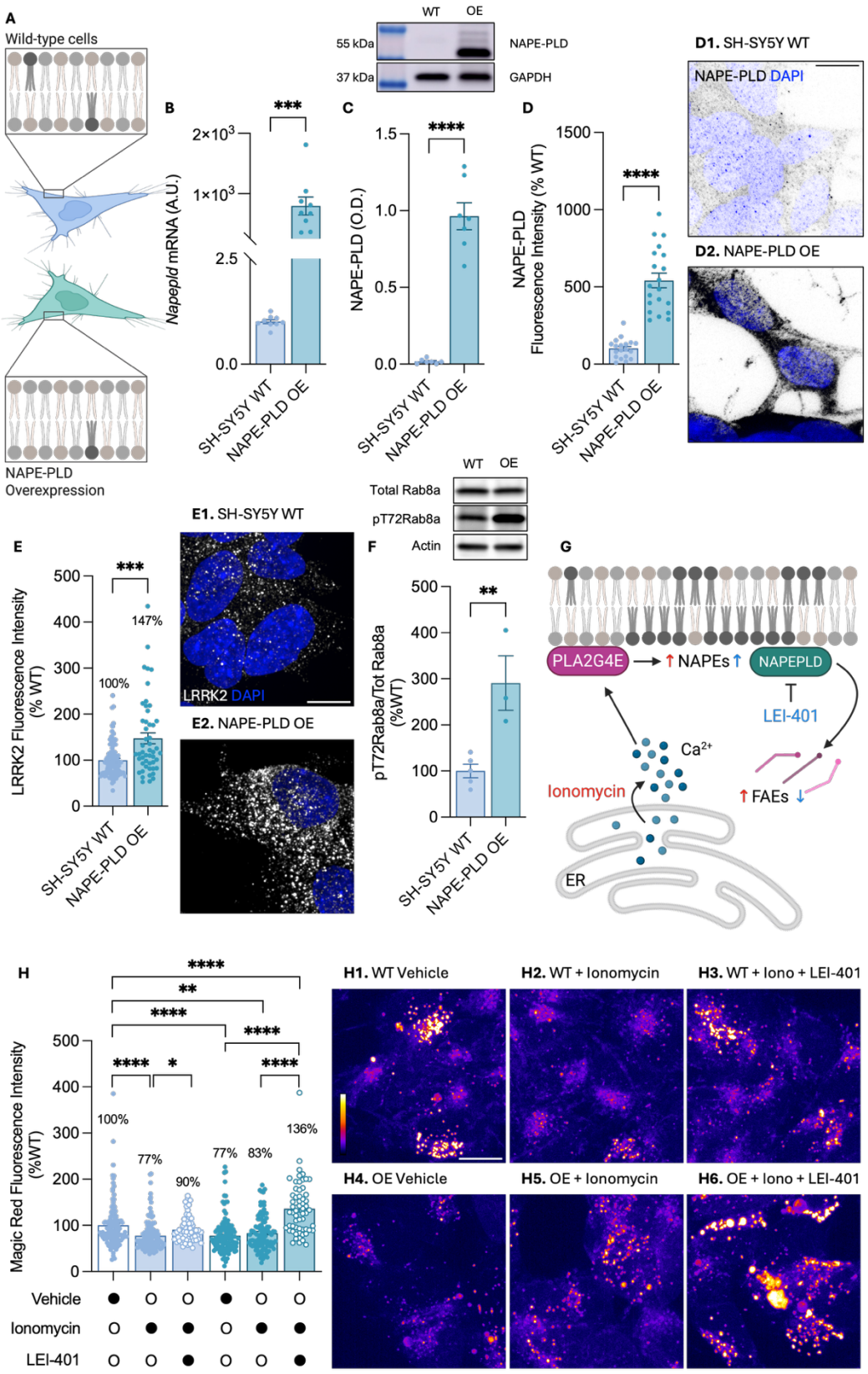
A
Wild-type cells
NAPE-PLD
Overexpression
B
Napepld mRNA (A.U.)
SH-SY5Y WT
NAPE-PLD OE
C
NAPE-PLD (O.D.)
WT
OE
55 kDa
37 kDa
NAPE-PLD
GAPDH
D
NAPE-PLD Fluorescence Intensity (% WT)
D1. SH-SY5Y WT
NAPE-PLD DAPI
D2. NAPE-PLD OE
E
LRRK2 Fluorescence Intensity (% WT)
147%
100%
E1. SH-SY5Y WT
LRRK2 DAPI
E2. NAPE-PLD OE
F
Total Rab8a
pT72Rab8a
Actin
pT72Rab8a/Tot Rab8a (%WT)
G
PLA2G4E
NAPEs
NAPEPLD
LEI-401
Ca2+
Ionomycin
FAEs
ER
H
Magic Red Fluorescence Intensity (%WT)
100%
77%
90%
77%
83%
136%
Vehicle
Ionomycin
LEI-401
H1. WT Vehicle
H2. WT + Ionomycin
H3. WT + Iono + LEI-401
H4. OE Vehicle
H5. OE + Ionomycin
H6. OE + Iono + LEI-401

725

Figure 4. NAPE-PLD overexpression upregulates LRRK2 protein and impairs lysosomal activity. (**A**) Schematic representation of the generation of stable SH-SY5Y cell lines overexpressing NAPE-PLD, leading to reduced NAPE levels at cellular membranes. (**B**) *NAPE-PLD* mRNA levels in NAPE-PLD-overexpressing (OE; green) and wild-type (WT; blue) cells. (**C**) Western blot analysis of NAPE-PLD protein levels in OE and WT cells. Top, representative blot; bottom, densitometric quantification normalized to GAPDH. (**D**) Immunofluorescence analysis of NAPE-PLD (gray) with representative images (**D1, D2**) and quantification. (**E**) Immunofluorescence analysis of LRRK2 (gray) with representative images (**E1, E2**) and quantification in WT (**E1**) and NAPE-PLD OE (**E2**) cells. Nuclei were counterstained with DAPI (blue). (**F**) Western blot analysis of Rab8a and phosphorylated Rab8a (pT72-Rab8a) in NAPE-PLD OE and WT cells. Top: representative blot; bottom, densitometric quantification normalized to actin. (**G**) Schematic representation of the experimental strategy. Ionomycin treatment induces intracellular Ca^{2+} release, promoting NAPE production and degradation in NAPE-PLD OE cells. NAPE-PLD activity was inhibited by overnight treatment with the NAPE-PLD inhibitor LEI-401. Ionomycin was administered together with Magic Red reagent for 30 min before image acquisition. (**H**) Fluorescence intensity quantification and representative images of the Magic Red – cathepsin B assay, indicating lysosomal degradative capacity per cell, in untreated WT (**H1,** white bar and blue dots) and NAPE-PLD OE cells (**H4,** white bar and green dots), ionomycin-treated WT (**H2,** blue bar and blue dots) and NAPE-PLD OE cells (**H5,** green bar and green dots) or WT (**H3,** blue bar white dots) and NAPE-PLD OE cells (**H6**, green bar and white dots) treated with ionomycin and LEI-401. Representative images are displayed using the FIRE lookup table (LUT) to indicate fluorescence intensity. Scale bars, 10 μm. Mean values are indicated in the graphs; error bars represent SEM. *P < 0.05, **P < 0.01, ***P < 0.001, ****P < 0.0001; Student's *t*-test with Welch's correction (**B-F**) and two-way ANOVA with Tuckey's multiple-comparisons test (**H**).

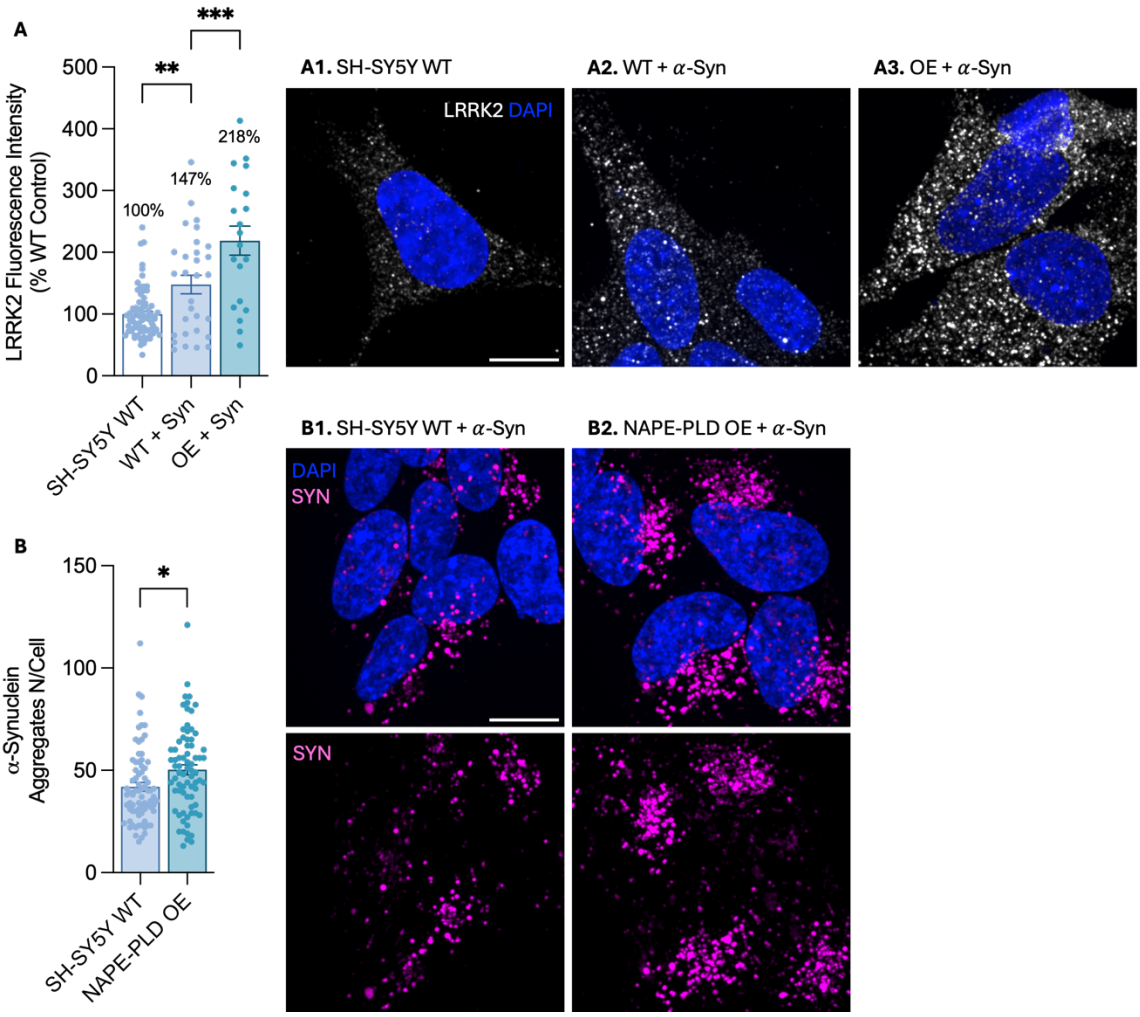

Figure 5. NAPE-PLD overexpression enhances LRRK2 accumulation following α-synuclein treatment and impairs aggregate clearance. (**A**) Immunofluorescence analysis of LRRK2 (gray) with representative images (**A1-A3**) and quantification in WT (**A1, A2**), and NAPE-PLD OE (**A3**) SH-SY5Y cells treated or not with α-synuclein (α-syn; **A2, A3**). (**B**) Quantification and representative images of α-syn aggregate number per cell in WT (**B1**) and NAPE-PLD OE (**B2**) cells. α-Syn is shown in pink, and nuclei were counterstained with DAPI. Scale bar, 10 μm. Mean values are indicated in the graphs; error bars represent SEM. *P<0.05, ***P < 0.001, ****P < 0.0001; one-way ANOVA with Tuckey's multiple-comparison test (**A**) and Student's *t*-test with Welch's correction (**B**).

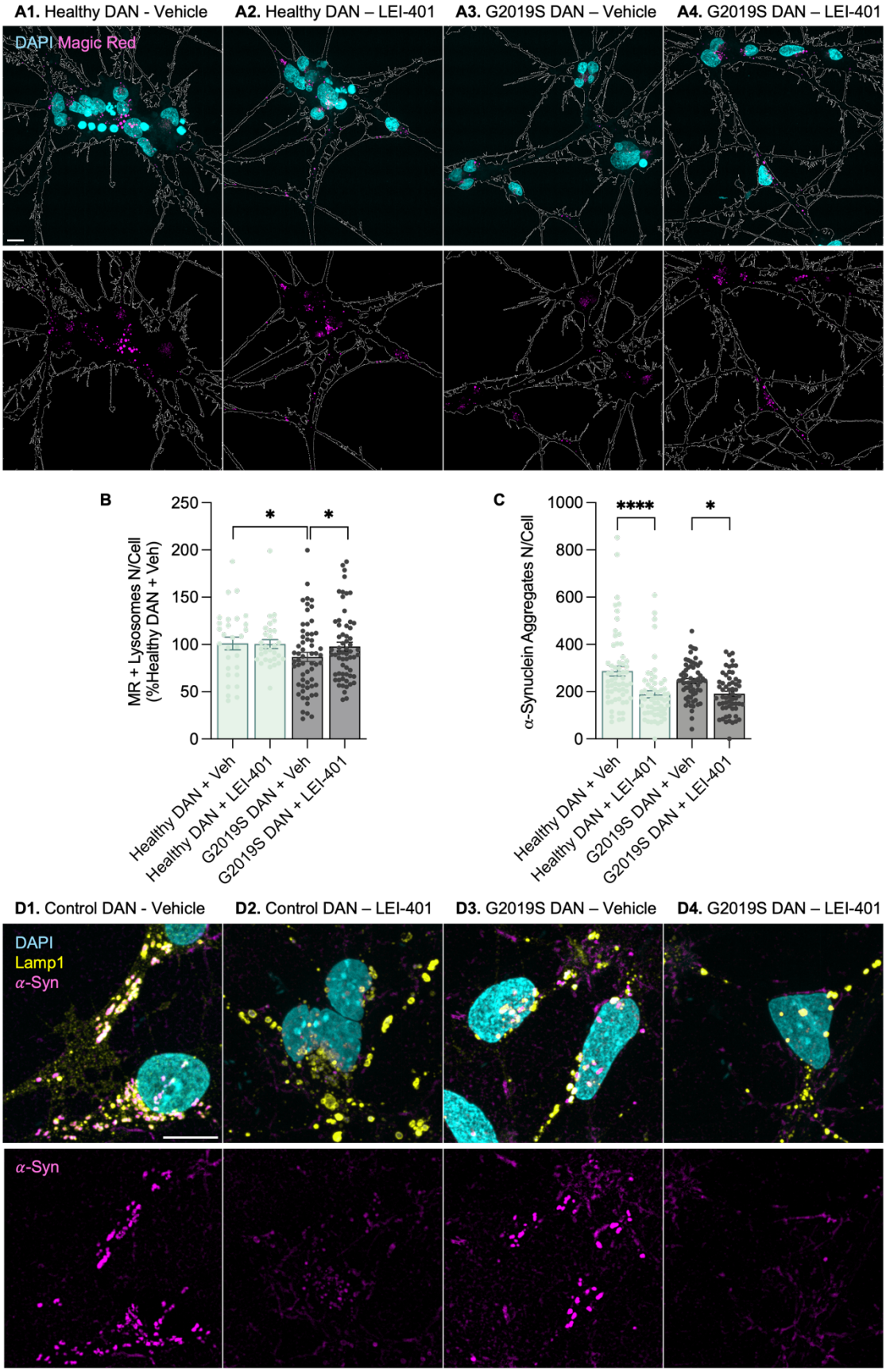
A1. Healthy DAN - Vehicle
A2. Healthy DAN – LEI-401
A3. G2019S DAN – Vehicle
A4. G2019S DAN – LEI-401
DAPI Magic Red
B
MR + Lysosomes N/Cell (%Healthy DAN + Veh)
250
200
150
100
50
0
*
*
Healthy DAN + Veh
Healthy DAN + LEI-401
G2019S DAN + Veh
G2019S DAN + LEI-401
C
α-Synuclein Aggregates N/Cell
1000
800
600
400
200
0
****
*
Healthy DAN + Veh
Healthy DAN + LEI-401
G2019S DAN + Veh
G2019S DAN + LEI-401
D1. Control DAN - Vehicle
D2. Control DAN – LEI-401
D3. G2019S DAN – Vehicle
D4. G2019S DAN – LEI-401
DAPI
Lamp1
α-Syn
α-Syn

762

763 **Figure 6. NAPE-PLD inhibition restores lysosomal activity and α-synuclein fibril clearance**
764 **in G2019S-LRRK2 dopaminergic neurons.** (**A**) Representative images of the Magic Red –
765 cathepsin B assay, indicating lysosomal degradative capacity per cell, in healthy dopaminergic
766 neurons (DANs; **A1, A2**) and G2019S-LRRK2 mutant DANs (**A3, A4**) treated (**A2, A4**) or not (**A1,**
767 **A3**) with the NAPE-PLD inhibitor LEI-401. (**B**) Fluorescence intensity quantification of the Magic
768 Red assay in healthy DANs (green) and G2019S-LRRK2 mutant DANs (gray). (**C, D**) Quantification
769 and representative images of α-synuclein (α-syn) aggregate number per cell in healthy DANs (**D1,**
770 **D2**) and G2019-LRRK2 mutant DANs (**D3, D4**) treated (**D2, D4**) or not (**D1, D3**) with LEI-401. α-
771 Syn is shown in pink, LAMP1 yellow, and nuclei were counterstained with DAPI. Scale bars, 10
772 μm. *P < 0.05, ****P < 0.0001; two-way ANOVA with Tuckey's multiple-comparison test.

773

774 ***Table 1:*** *Primers used in the study.*

Gene	Forward primer	Reverse primer
NAPE-PLD	GGACATCAGTGTGAATCCTTACAG	GGACATCAGTGTGAATCCTTACAG
PLA2G4E	GATGCCTGGAACCTGTCACACA	TCACTACCGTGGTCTCCAGGAT
GAPDH	GTCTCCTCTGACTTCAACAGCG	ACCACCCTGTTGCTGTAGCCAA
ACTINB	CACCATTGGCAATGAGCGGTTC	AGGTCTTTGCGGATGTCCACGT
HPRT	CATTATGCTGAGGATTTGGAAAGG	CTTGAGCACACAGAGGGCTACA

775
776

777 ***Table 2:*** *Parent, quantifier and qualifier ions (as m/z) tracked for each of the 14 NAPEs under*
778 *investigation. The corresponding observed retention time (in minutes) is also indicated.*

ID	NAME	Parent m/z	Fragment m/z (Qn)	Fragment m/z (Qf)	Rt (min)
1	PE (P50:1-N-acyl)	940.8	282.3	561.5	5.03
2	PE (P52:2-N-acyl)	966.8	282.3	587.5	5.03
4	PE (P54:5-N-acyl)	988.8	282.3	609.5	4.79
5	PE (P54:4-N-acyl)	990.8	282.3	611.5	5.00
7	PE (P50:6-N-acyl)	1014.8	308.3	609.5	4.81
10	PE (P50:5-N-acyl)	1016.8	308.3	611.5	5.01
11	PE (P50:5-N-acyl)	1016.8	310.3	609.5	5.00
20	PE (P50:6-N-acyl)	1014.8	282.3	635.5	4.92
21	PE (P50:6-N-acyl)	1014.8	310.3	607.5	4.92
22	PE (50:6-N-acyl)	1030.8	282.3	651.5	4.84
23	PE (50:6-N-acyl)	1030.8	310.3	623.5	4.82
24	PE (50:4-N-acyl)	1034.8	310.3	627.5	5.10
25	PE (P58:6-N-acyl)	1042.8	310.3	635.5	4.98
26	PE (58:6-N-acyl)	1058.8	310.3	651.5	5.03

779
780